Ultrasonic monitoring of spontaneous imbibition experiments: Acoustic signature of fluid migration

Christian David, Christophe Barnes, Mathilde Desrues, Lucas Pimienta, Joël Sarout, Jérémie Dautriat

AGU PUBLICATIONS

JGR

Journal of Geophysical Research: Solid Earth

RESEARCH ARTICLE
10.1002/2016JB013804

Special Section:
Seismic and micro-seismic signature of fluids in rocks: Bridging the scale gap

This article is a companion to *David et al.* [2017] doi:10.1002/2017JB014193.

Key Points:
- A comprehensive data set of imbibition tests with ultrasonic monitoring and CT scan imaging is presented for sandstone and carbonate rocks
- The interplay between fluid motion and variations in waveform attributes (velocity, amplitude, spectral content, and energy) is analyzed
- A method based on the instantaneous frequency is used to decompose the waveforms into wavelets which are impacted by fluid substitution in different ways

Supporting Information:
- Supporting Information S1
- Movie S1
- Movie S2
- Movie S3
- Movie S4

Correspondence to:
C. David,
christian.david@u-cergy.fr

Citation:
David, C., C. Barnes, M. Desrues, L. Pimienta, J. Sarout, and J. Dautriat (2017), Ultrasonic monitoring of spontaneous imbibition experiments: Acoustic signature of fluid migration, *J. Geophys. Res. Solid Earth*, *122*, 4931–4947, doi:10.1002/2016JB013804.

Received 29 NOV 2016
Accepted 30 MAR 2017
Accepted article online 29 JUN 2017
Published online 18 JUL 2017

Ultrasonic monitoring of spontaneous imbibition experiments: Acoustic signature of fluid migration

Christian David[1], Christophe Barnes[1], Mathilde Desrues[1,2], Lucas Pimienta[3], Joël Sarout[4], and Jérémie Dautriat[4]

[1]Laboratoire Géosciences et Environnement Cergy, Université de Cergy-Pontoise, Cergy-Pontoise, France, [2]EOST, Université de Strasbourg, Strasbourg, France, [3]Laboratoire de Géologie de l'ENS-PSL Research University-UMR8538 du CNRS, Paris, France, [4]CSIRO Energy, Perth, Western Australia, Australia

Abstract Capillary rise experiments (spontaneous imbibition tests) were conducted in the laboratory with ultrasonic and X-ray monitoring on the Sherwood sandstone and the Majella grainstone. The aim was to provide a direct comparison between the variation in seismic attributes (amplitude, velocity, spectral content, and energy) and the actual fluid distribution in the rock. Two pairs of ultrasonic *P* wave sensors located at different heights on a cylindrical rock specimen recorded every 5 s the waveforms when capillary forces make water rise up into the rock from the bottom in contact with a water tank. Simultaneously, computerized tomography scan images of a vertical cross section were also recorded. Two important results were found. (i) The amplitude of the first *P* wave arrival is impacted by the upward moving fluid front before the *P* wave velocity is, while the fluid front has not yet reached the sensors level. In contrast, the *P* wave velocity decreases when the fluid front reaches the Fresnel clearance zone. The spectral analysis of the waveforms shows that the peak frequency amplitude is continuously decreasing without noticeable frequency shift. (ii) A methodology based on the calculation of the analytical signal and instantaneous phase was designed to decompose each waveform into discrete wavelets associated with direct or reflected waves. The energy carried by the wavelets is very sensitive to the fluid substitution process: the coda wavelets related to reflections on the bottom end face of the specimen are impacted as soon as imbibition starts and can be used as a precursor for the arriving fluid.

1. Introduction

Fluid substitution processes in porous media are investigated in different scientific research fields because they can lead to significant modifications in the physical properties of the medium. This is particularly true in Earth sciences, in the area of gas and oil recovery [*Doornhof et al.*, 2006], groundwater management [*Novakowski and Gillham*, 1988], CO_2 sequestration [*JafarGandomi and Curtis*, 2011], and geothermal energy extraction [*Jaya et al.*, 2008]. As the elastic properties of reservoir rocks are highly sensitive to the nature of the fluids saturating the pore space [*Mavko et al.*, 2009; *Rasolofosaon and Zinszner*, 2012], remote seismic monitoring has been proposed as a tool to characterize fluid substitution processes in reservoirs [*Rasolofosaon and Zinszner*, 2004]. Successful laboratory studies were conducted by *Wulff and Mjaaland* [2002] looking at reflected seismic waves in a block of sandstone flooded by water and by [*Stanchits et al.*, 2011] in fluid injection experiments with acoustic emissions recording and ultrasonic monitoring. Recently, *David et al.* [2015a] and [*Dautriat et al.*, 2016] showed that water injection into a weakly consolidated sandstone saturated with oil or under dry conditions resulted in a decrease of *P* wave velocity, whereas oil injection into the dry rock resulted in an increase of *P* wave velocity: this striking difference was explained by the wetting contrast between both injected fluids, leading in the former case to a patchy saturation, and also by an elastic weakening effect of the water (reduction in *P* wave velocity) also referred to as chemical weakening [*Mavko et al.*, 2009]. In their experimental work, [*Baud et al.*, 2000] explained the mechanical and elastic weakening observed for water-saturated sandstones by physico-chemical interactions when water is adsorbed at grain boundaries, leading to a reduction of surface energy. Water-weakening effects have been well documented for a variety of rocks, especially sandstones [*Hadizadeh and Law*, 1991] and carbonate rocks [*Rutter*, 1972; *Risnes et al.*, 2005]. In addition to the weakening effect of water as a liquid phase in a porous rock, water vapor has also a strong elastic weakening effect when adsorbed at mineral surfaces and/or grain contacts. *Pimienta et al.* [2014] investigated a set of sandstones and limestones and found significant variations of seismic attributes (*P* wave and *S* wave velocity and amplitude) in the loosely cemented sandstones

Table 1. Mineralogical Composition and Petrophysical Properties of the Rocks [*Baud et al*., 2009; *Nguyen et al*., 2014; *David et al*., 2015a][a]

	Majella Grainstone	Sherwood Sandstone
Mineralogical composition	Pure calcite	Quartz (30%), feldspar (18%), clays (12%), mica (7%), heavy minerals (3%), void (30%)
Porosity	30%	30%
Mean grain size	54 μm	120 μm
Mean throat size from MICP	16 μm	18 μm
Permeability	450 mD	200–350 mD
P wave velocity (dry)	2100–2900 m/s	1400–1800 m/s
P wave velocity (water saturated)	2800–3400 m/s	~2000 m/s

[a]The range of *P* wave velocity corresponds to the variability related to anisotropy. MICP, Mercury Injection Capillary Pressure.

when changing the relative humidity: in such experiments the water saturation is very low and the observed effects are due to moisture diffusion in the pore space. A grain contact model [*Digby*, 1981] modified to include the effect of surface energy reduction by moisture adsorption accounted well for these observations [*Pimienta et al*., 2014]. In order for a remote monitoring method to be efficient and predictive, the variations in seismic properties need to be related to the actual fluid distribution in the porous medium [*Avseth et al*., 2005]. Imaging techniques can be used to link the geometrical properties of the pore space to its seismic attributes. At the laboratory scale, this can be achieved using X-ray imaging, a technique widely used nowadays for imaging porous rocks [*Mees et al*., 2003]. For example, water injection tests with ultrasonic monitoring were conducted under a medical X-ray computed tomography (CT) scanner to link the ultrasonic attributes to the water saturation derived from X-ray CT density maps, for different injection rates [*Lopes et al*., 2012, 2014]. Recently, *David et al*. [2015b] recorded the *P* wave waveforms with two pairs of sensors while simultaneously acquiring X-ray CT images during spontaneous imbibition experiments on two carbonate rocks. They showed that the *P* wave amplitude systematically decreased before the *P* wave velocity was impacted by the arrival of the water front. Furthermore, this amplitude decrease occurred when the fluid front was well below the location of the ultrasonic sensors. Whereas the relationship between the fluid front position and the onset of velocity decrease could be explained by taking into account the size of the Fresnel clearance zone [*Spetzler and Snieder*, 2004], no explanation was found for the decoupled evolution of *P* wave amplitude and velocity. It was concluded that the *P* wave amplitude (related to the *P* wave attenuation) is more sensitive to fluid substitution processes than the *P* wave velocity, in agreement with the results of *Wulff and Mjaaland* [2002].

In the present work we address the following questions. Can fluid substitution processes be detected by remote ultrasonic methods at the laboratory scale? How does fluid substitution modify waveforms and spectral contents of remotely recorded seismic signals? Which seismic attributes are the most appropriate for detecting fluid substitution effects in reservoir rocks? Does a full waveform analysis including a detailed analysis of the energy carried by the waveform coda provide information on ongoing fluid substitution processes? To answer these questions, we developed an experimental methodology combining rock physics, seismic signal processing, and X-ray CT imaging applied to spontaneous water imbibition experiments, in which capillary forces make water rise into a rock sample in contact with a water tank.

2. Selected Rock Material

Two rocks were selected for this study, a sandstone rock and a carbonate rock, which were both studied in previous works. Therefore, an extensive data set on their mineralogical composition and petrophysical properties was already available (Table 1). Both rocks are anisotropic: the impact of anisotropy on spontaneous imbibition tests has been studied in a previous work [*David et al*., 2011].

2.1. Sherwood Sandstone

The Triassic Sherwood Sandstone is poorly consolidated with a heterogeneous mineralogical content. It outcrops in the South-West shore of England and was directly sampled from Ladram Bay cliffs. This sandstone

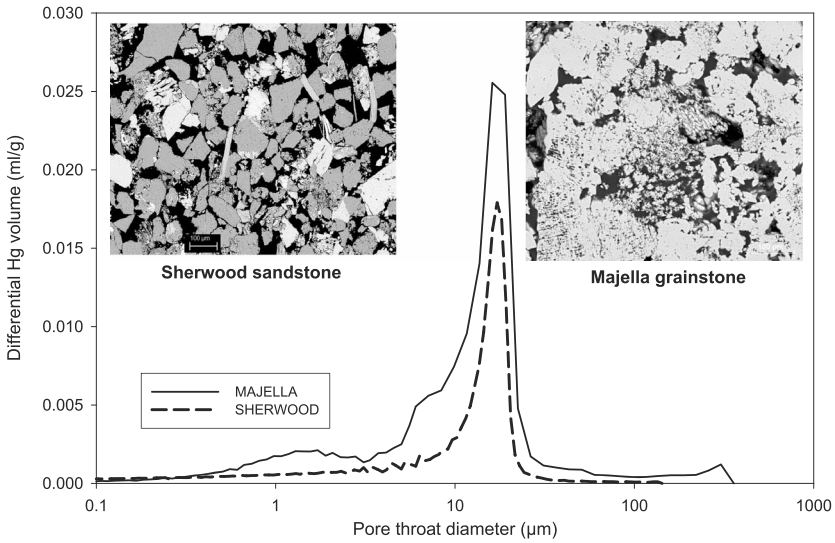

Figure 1. Pore throat diameter distribution from mercury injection tests and SEM micrographs for both rocks.

belongs to the group of reservoir rocks of the nearby onshore Wytch Farm Oil Field in Dorset, produced at a depth of approximately 1500 m. Quartz, feldspar, and clays are the major minerals in the rock composition. The Sherwood sandstone has a mean porosity of 30% and an average grain diameter of 120 μm. The pore throat distribution obtained by mercury injection is relatively narrow with a peak at 18 μm diameter and a long tail toward low values down to 0.1 μm (Figure 1). The permeability is anisotropic: 200 mD and 350 mD, normal and parallel to the bedding, respectively. The sample tested in this work comes from the same block investigated in previous studies on Sherwood sandstone [*Nguyen et al*., 2014; *David et al*., 2015b; *Dautriat et al*., 2016]. The dry Sherwood sandstone has a significant velocity anisotropy (about 25%) with a minimum *P* wave velocity perpendicular to the bedding (1400 m/s) and a maximum velocity parallel to bedding (1800 m/s) at room conditions. This anisotropy vanishes when the rock sample is fully saturated with water (V_P ~ 2000 m/s). The evolution of *P* wave velocity for partially saturated samples shows that in the low-water saturation range ($S_w < 55\%$), the *P* wave velocity is lower than that of the dry rock and then increases to higher values close to full saturation [*Dautriat et al*., 2016]. *P* wave velocity anisotropy and variation with saturation are expected to impact the results reported below.

2.2. Majella Grainstone

The Majella grainstone comes from the Madonna delle Mazze quarry in the Apennines (Central Italy), situated on the inner part of the forelimb of the Majella Anticline. Our sample comes from a block of undeformed host rock outcropping in the quarry, the same as the one tested by *Baud et al*. [2009]. The Majella grainstone is a pure calcite grainstone formed from rudist bivalve fragments with no preferred spatial orientation. The average porosity is 30%, and the grain size is variable from a few microns to a few millimeters with an average grain diameter of ~ 54 μm. The pore size distribution spreads over a large range with a main peak at diameter 16 μm and a secondary peak near 2 μm (Figure 1). The permeability of the Majella grainstone measured on the outcrop in the quarry by *Tondi et al*. [2016] was 450 mD in average. The *P* wave velocity varies between 2100 and 2900 m/s for the dry Majella grainstone (anisotropy 27%) and between 2800 and 3400 m/s for the water-saturated rock (anisotropy 18%) [*Baud et al*., 2009].

3. Methodology

Following the methodology presented in *David et al*. [2015b], spontaneous imbibition experiments with ultrasonic monitoring and X-ray imaging were conducted on both rocks.

3.1. Experimental Setup

The experimental setup and the location of the ultrasonic sensors glued on the sample surface are shown in Figure 2. The rock samples are placed on an X-ray transparent stand providing a constant water level at the

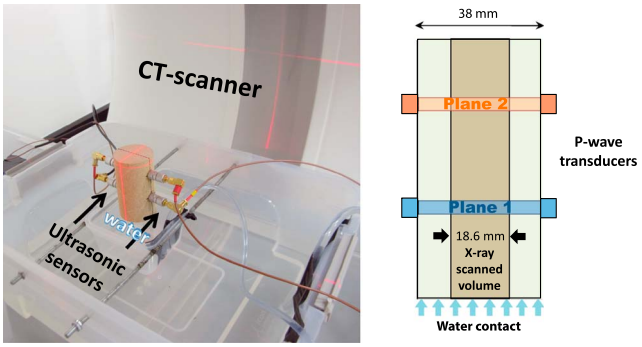

Figure 2. Experimental setup for the imbibition tests with X-ray imaging coupled with ultrasonic measurements.

bottom end of the cylindrical rock specimen. The rock samples have a diameter of 38 mm and a length of approximately 80 mm. Two pairs of ultrasonic sensors are glued with cyanoacrylate at two different heights spaced 25 mm apart. Each sensor is made of a piezoelectric lead zirconate titanate (PZT) 5 mm in diameter encapsulated in an aluminum holder (in-house design) with 9 mm external diameter. The surface of the holder in contact with the rock is machined concave so as to match the cylindrical lateral surface of the specimen. The mean resonant frequency of the PZTs is ~0.5 MHz. The PZTs are connected by coaxial wires to a switch box and a digital oscilloscope, which record the signal with a sampling frequency of 10 MHz. In the following analysis we will consider each source-receiver pair in planes 1 and 2 independently (Figure 2).

During the imbibition test, the sample's volume is continuously scanned with an X-ray CT scanner (Siemens SOMATOM Dual Energy 64 slices). A 140 kV/300 mA single X-ray energy beam was used, and a typical acquisition set is made of 32 parallel and simultaneous slices separated by 0.6 mm in the central part of the sample. To avoid artifacts related to the ultrasonic transducers interacting with the X-ray beams, the sample is imaged along vertical planes normal to the plane defined by the positions of the four transducers (Figure 2). The investigated volume is therefore a truncated cylinder 18.6 mm in width. Each scanning stage lasts 1 s and is repeated every 5 s. The pixel size in each reconstructed image is 0.15 mm × 0.15 mm. At each X-ray scanning stage, waveforms transmitted through the rock specimen between the emitting and the receiving ultrasonic transducers are recorded.

3.2. Measurement of Seismic Attributes (*P* Wave Velocity and Amplitude)

The waveforms captured by the receivers are sent to a digital oscilloscope (100 MHz sampling frequency). The received waveforms are manually recorded on a memory stick every 5 s. After the experiment, the waveforms are analyzed with a program written using Scilab. Two parameters are automatically retrieved from each recorded waveform: (i) the *P* wave arrival time from which the phase velocity is obtained and (ii) the amplitude of the first peak. For picking automatically the first *P* wave arrival, we used the Akaike information criterion [*Akaike*, 1974], a robust technique commonly used is seismology. Amplitude variations are a manifestation of attenuation and/or scattering of *P* wave energy [*Bourbié et al*., 1987]. *P* wave attenuation is generally quantified by estimating the quality factor *Q* using, for example, the spectral ratio method [*Toksöz et al*., 1979]. For sake of simplicity our method consists in picking the amplitude of the first peak in the recorded waveforms. Doing so, our goal is not to quantify attenuation but to track any amplitude variation when the properties of the studied materials are changing.

3.3. Waveform Analysis

Additional insight into the dynamics of fluid propagation within the rock can be obtained by plotting the evolution of the waveforms recorded during water imbibition, as well as the evolution of the corresponding frequency spectra (Figure 3). Parameters like phase shift δt, amplitude loss δA, and the trajectory of the peak frequency in the Fourier domain can be characterized dynamically.

A very efficient way to illustrate the impact of the moving fluid front consists in building a movie from the sequence of snapshots acquired during imbibition. Each snapshot consists of the waveform, the associated frequency spectrum, and the corresponding X-ray CT image showing the fluid front. In such a movie, the

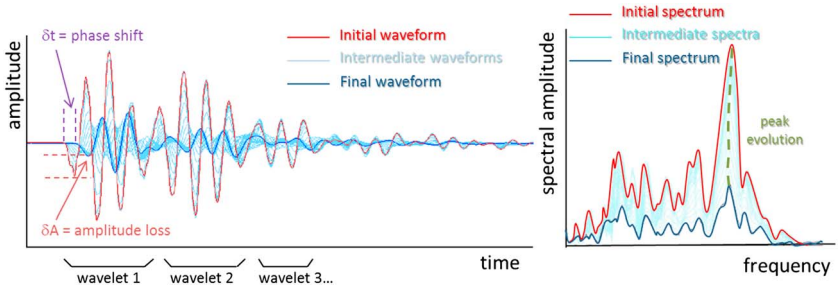

Figure 3. Example of waveforms recorded during an imbibition experiment with associated frequency content in the Fourier domain. Phase shift, amplitude loss, and peak frequency path can be estimated from such a plot.

evolution of the waveform attributes with the knowledge of the position of the fluid front in the rock can be easily visualized. These movies are provided as supporting information on the journal's website.

3.4. Wavelet Analysis

It is generally possible to identify several wavelets in a given waveform recorded during imbibition (Figure 3). In order to identify and isolate each wavelet from the complete waveform, a method was designed based on the calculation of the analytical signal [*Bracewell*, 2000] and the instantaneous frequency [*Cohen*, 1995]. Similar methods based on the determination of the instantaneous frequency have been used in seismics [*Taner et al*., 1979; *Barnes*, 1992], biological sciences for the analysis of ultrasonic signals in bones [*Nagatani and Tachibana*, 2014] and of electroencephalograms [*Boashash et al*., 2012]. None of these studies had the same objective as ours, the decomposition of the waveforms into several wavelet packets. Let us call $w(t)$ the recorded waveform: we first calculate the corresponding analytical signal

$$w_a(t) = w(t) + i.H_w(t) \tag{1}$$

where $H_w(t)$ is the Hilbert transform of the waveform

$$H_w(t) = \frac{1}{\pi} p.v. \int_{-\infty}^{+\infty} \frac{w(\tau)}{t-\tau} \mathrm{d}\tau \tag{2}$$

where *p.v.* stands for Cauchy principal value. Writing $w_a(t) = A(t)\,.\,e^{i\phi(t)}$, we define the instantaneous amplitude or envelop $A(t)$ and the instantaneous phase $\phi(t)$ [*Cohen*, 1995] from which the unwrapped phase $\phi_u(t)$ is calculated. The instantaneous frequency $f_{\mathrm{inst}}(t)$ is related to $\phi_u(t)$ by

$$f_{\mathrm{inst}} = \frac{1}{2\pi} \frac{\mathrm{d}\phi_u(t)}{\mathrm{d}t} \tag{3}$$

When plotting the unwrapped phase and instantaneous frequency versus time (Figure 4), one generally observes linearity on the phase plot over distinct time intervals, corresponding approximately to a constant value for the instantaneous frequency. The limits between those intervals are usually (but not necessarily) associated with a reversal of the spikes polarity on the frequency plot [*Hsu et al*., 2011].

Our method is based on the identification of such intervals: each of them will be considered as belonging to a specific wavelet packet composed of phase and frequency consistent wavelets. The significance of such wavelet packet needs to be elucidated, taking into account the boundary conditions for wave propagation in the cylindrical rock sample. Each wavelet packet can be studied independently by applying an apodization window on the recorded waveform. For the apodization procedure we used a Hamming zero mean time window slightly larger than the detected intervals in Figures 9 and 10 with the possibility to adjust the position of the window if phase shifts become too large during the imbibition process. The aim of the wavelet decomposition is to decipher the complexity of the recorded waveforms and their evolution during the imbibition process. The wavelet decomposition of the recorded waveform is expected to reflect the direct propagation and multiple reflections within the rock sample of the ultrasonic vibration generated by the source transducer and eventually reaching the ultrasonic receiver. Each of these wavelet packets is therefore expected to carry information about different parts of the rock sample and in particular the fluid distribution there. These aspects are addressed in section 5.

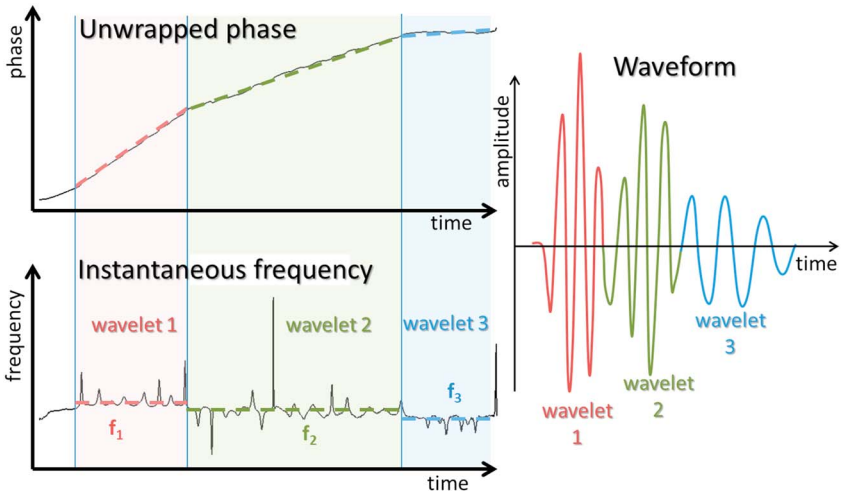

Figure 4. Sketch of the method used to identify wavelets in the recorded waveforms.

The instantaneous frequency is also used to estimate the width R_F of the first Fresnel zone defined in wave propagation theory [*Červený and Soares*, 1992; *Spetzler and Snieder*, 2004; *David et al*., 2015b]. This zone can be approximated for homogeneous and isotropic media by an ellipsoid with a major axis equal to half the distance D between the sensors and minor axes R_F given by the following relation:

$$R_F = 0.5\sqrt{\lambda D + \frac{\lambda^2}{4}} \tag{4}$$

where the wavelength λ is estimated by the ratio between the P wave velocity and the instantaneous frequency. The ultrasonic wave propagating in the rock between the source and the receiver is impacted by heterogeneities (migrating fluid) located in the Fresnel clearance zone of maximum half-width R_F. These heterogeneities will therefore impact the wave velocity and amplitude as recorded in the waveforms.

4. Results

First, we analyze the capillary rise kinetics and how it impacts the P wave velocity and amplitude. Second, we show how the waveforms and associated spectra change dynamically during imbibition. Finally, the recorded signals are analyzed in terms of wavelets and corresponding propagation paths and how each wavelet is impacted (or not) by the presence of the moving fluid front.

4.1. Capillary Rise and Ultrasonic Monitoring

4.1.1. Sherwood Sandstone

The X-ray CT images reveal that the Sherwood sandstone is finely layered, with alternating dark and bright horizontal layers (Figure 5), the brighter layers (higher density) being thinner than the darker zones (lower density). The red dashed line in Figure 5c shows the position of the identified interface between the water-invaded volume (brighter because of the density increase) and the allegedly dry part of the sample. Using standard computer routines available in the ImageJ freeware, the maximum height of the water front is automatically detected on each image after contrast enhancement. The resulting height increase with the square root of time is shown in Figure 5a. As discussed by *David et al*. [2011], capillary rise is a diffusive process; therefore, it is more convenient to use the square root of time for the x axis (e.g., in a capillary pipe fluid rises linearly with the square root of time). For the Sherwood sandstone the height increase is not linear, probably due to the layered structure of the material. Two average slopes can be determined, one in the early stages of imbibition (1.14 mm/s$^{1/2}$ with R^2 = 0.982) and another one after the water front has reached a height of ~ 20 mm (0.690 mm/s$^{1/2}$ with R^2 = 0.997). The evolution of the P wave amplitude and velocity for the ultrasonic source-receiver pairs in planes 1 and 2 (Figure 2), normalized by their initial value, are shown in Figure 5b. The initial P wave velocity is 1740 m/s in plane 1 and 1630 m/s in plane 2. In both planes, velocity decreases monotonically upon the arrival of the imbibition front. In plane 2, the wave amplitude also decreases monotonically; however, in plane 1 the wave amplitude oscillates at the early stages of imbibition before reaching a monotonic decreasing trend.

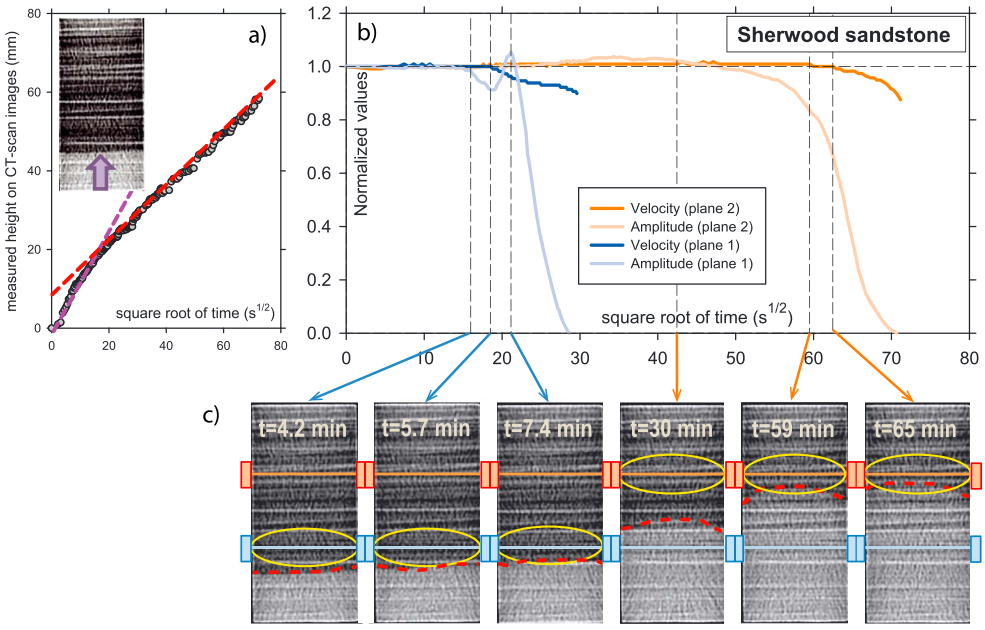

Figure 5. Results for the Sherwood sandstone. (a) Water height versus square root of time. (b) Variation of *P* wave velocity and first peak amplitude versus square root of time. (c) CT scan images at selected times during the imbibition process. For scale reference the rock specimen imaged is 38 mm wide. Ultrasonic monitoring planes 1 and 2 (lines) and corresponding sensors (rectangles) are represented in blue and orange, respectively.

Let us now compare the *P* wave attributes and the position of the imbibition front as determined in the X-ray CT images. The location of each transducer and the investigated plane are shown on each image. The vertical extent of the Fresnel clearance zone is shown by the ellipse with R_F = 8 mm (Figures 5b and 5c). For sake of clarity, the imbibition process is decomposed into six stages:

Stage 1 The wave amplitude in plane 1 decreases, whereas the wave velocity remains unchanged. The imbibition front is below the lower boundary of the Fresnel zone.

Stage 2 The velocity in plane 1 decreases, whereas the amplitude reverses to an increasing trend. This seems to occur when the water front reaches the lower boundary of the Fresnel zone.

Stage 3 The amplitude reverses again to a decreasing trend, seemingly when the imbibition front reaches the lower boundary of the transducers zone.

Stage 4 The amplitude in plane 2 decreases monotonically, while the imbibition front is still located well below the Fresnel zone. The amplitude in plane 1 becomes vanishingly small, and the picking of *P* wave traveltime is no more possible.

Stage 5 The velocity in plane 2 decreases when the imbibition front is within the Fresnel zone and reaches the lower boundary of the transducers zone.

Stage 6 Both amplitude and velocity in plane 2 are decreasing sharply when the imbibition front is within the transducers zone. The amplitude drops to zero and no traveltime picking is possible.

4.1.2. Majella Grainstone

A similar analysis is conducted on the Majella grainstone (Figure 6). The X-ray CT images show that the Majella grainstone is heterogeneous, with dense oblique features crossing the sample (Figure 6c). In contrast with the Sherwood sandstone (Figure 5a), the height plot in Figure 6a is linear throughout the experiment, with an average slope of 1.58 mm/s$^{1/2}$ with R^2 = 0.996. Figure 6b shows that the time evolution of the normalized *P* wave amplitude and velocity in the Majella grainstone is qualitatively similar to that of the Sherwood sandstone (Figure 5b). The initial velocity is 2290 m/s in plane 1 and 2260 m/s in plane 2. The Fresnel clearance zone is characterized by an ellipse with R_F = 8.5 mm (Figure 6c). For sake of clarity, the imbibition process is decomposed into five stages:

Stage 1 The wave amplitude sharply decreases in plane 1, whereas the wave velocity remains unchanged. The imbibition front reaches the lower boundary of the Fresnel zone. In contrast with the

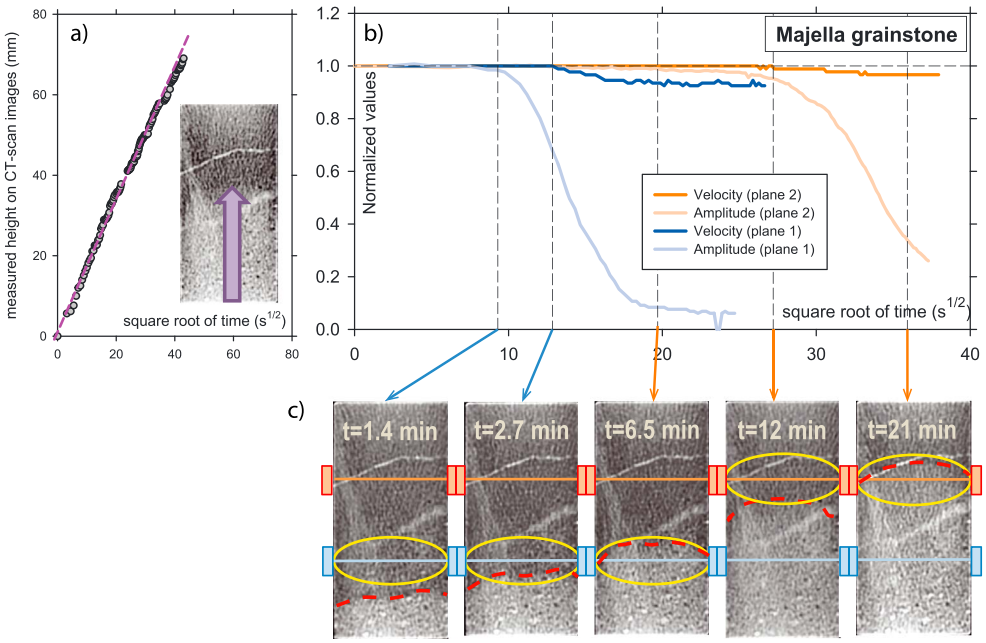

Figure 6. Results for the Majella grainstone. (a) Water height versus square root of time. (b) Variation of *P* wave velocity and first peak amplitude versus square root of time. (c) CT scan images at selected times during the imbibition process. For scale reference the rock specimen imaged is 38 mm wide. Ultrasonic monitoring planes 1 and 2 (lines) and corresponding sensors (rectangles) are represented in blue and orange, respectively.

Sherwood sandstone, no fluctuation of the amplitude at the early stages of the imbibition is observed in the Majella grainstone.

Stage 2 The velocity in plane 1 decreases, while the water front is located within both the Fresnel zone and the transducers zone.

Stage 3 The amplitude in plane 2 decreases slowly, whereas the velocity remains unchanged. The imbibition front lags far below the corresponding Fresnel zone. As the water front is now well ahead of the transducers zone for plane 1, no significant velocity variation is observed.

Stage 4 The velocity in plane 2 decreases, while the imbibition front reaches the lower boundary of the Fresnel zone. The amplitude drops faster.

Stage 5 The amplitude in plane 2 keeps on decreasing, whereas the velocity reaches a plateau. The top of the water front is located just beyond the upper boundary of the transducers zone.

4.2. Waveform Analysis

4.2.1. Sherwood Sandstone

The complete set of waveforms recorded on planes 1 and 2 in the Sherwood sandstone are plotted in Figure 7. Several features can be highlighted as follows:

1. The moving fluid front and time-dependent water saturation have a very strong impact on the amplitude and spectral content of the waveforms.
2. The waveforms and spectra recorded on both planes are significantly different.
3. In the early stages of imbibition a peak frequency between 360 and 390 kHz is observed in the spectra from plane 1. The trajectory of the peak in this graph shows an amplitude increase (red dashed line), followed by a decrease (blue dashed line). In plane 2 a monotonic decrease is observed.
4. As imbibition proceeds, the high-frequency peak becomes weaker, and by the end of the imbibition the waveforms are dominated by low frequencies.
5. Except for the very first arrivals, there is little phase shift in the signals recorded in plane 1 compared to plane 2 where phase shifts are observed at all times.
6. Looking for plane 1 at the first three stages identified in the previous section, the waveforms are well correlated except for the phase shift on the first arrival: the main feature observed is the amplitude variations of the different arches.

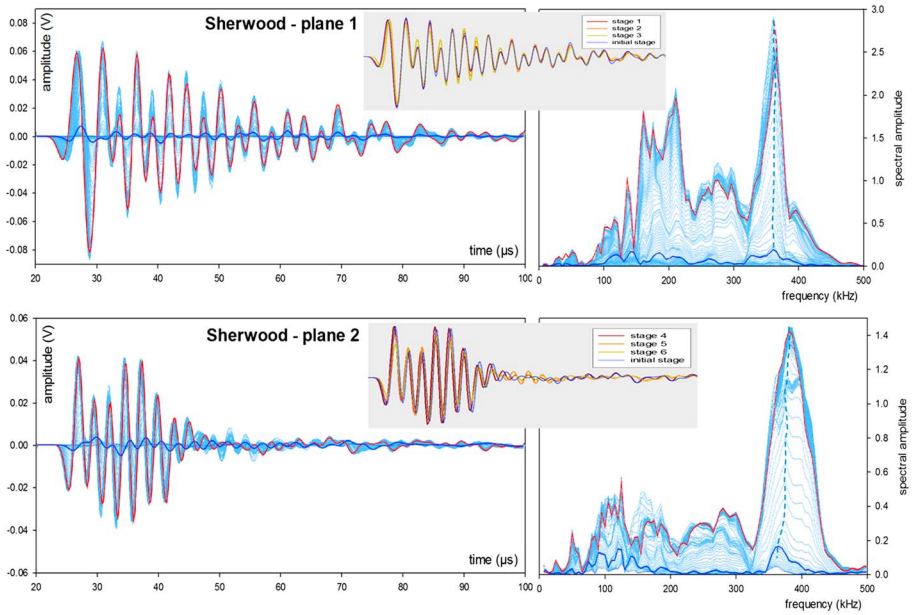

Figure 7. Plot of all the waveforms recorded during spontaneous water imbibition of the (left column) Sherwood sandstone and (right column) associated spectral amplitude for the transducers in (top row) plane 1 and (bottom row) plane 2. The red curves represent the initial stage (dry rock), and the dark blue curves represent the final stage approaching the time at which the signal vanishes. The inserted graphs show the waveforms corresponding to the six snapshots in Figure 5.

7. Looking for plane 2 at the last three stages, more phase shifts are observed and the waveforms recorded are less correlated: after about 40 μs, significant changes in both phase and amplitude are observed from one stage to the other.

4.2.2. Majella Grainstone

A similar analysis was conducted on the Majella grainstone (Figure 8). The main observations are as follows:

1. Again, the moving fluid front and time-dependent water saturation have a very strong impact on the amplitude and spectral content of the waveforms.
2. The waveforms and spectra recorded in each plane are consistent.
3. In the early stages of imbibition a peak frequency between 350 and 370 kHz is observed in the spectra from plane 1: the amplitude of this peak is strongly reduced during the imbibition, and the waveforms are dominated by low frequencies by the end of the experiment.
4. In contrast with the Sherwood sandstone, concomitant amplitude variations and phase shifts are observed throughout the experiment in the Majella grainstone.
5. For the first three stages identified in the previous section, the first arrivals in plane 1 are impacted starting at stage 2, but late arrivals are impacted already at stage 1; the waveform recorded at stage 3 has a much lower frequency content.
6. For the last three stages, stage 3 has no impact at all on the waveforms in plane 2; stage 4 only impacts significantly the arrivals after 40 μs, and the waveforms at stage 5 have a strong reduction both in amplitude and frequency content.

4.3. Wavelet Analysis

The method described in section 3.4 was applied to the waveforms acquired on the dry samples before the spontaneous water imbibition starts. Five wavelet packets could be identified for the Sherwood sandstone and seven for the Majella grainstone. The main attributes of these wavelet packets are summarized in Table 2.

4.3.1. Sherwood Sandstone

Figure 9 presents the unwrapped instantaneous phase and the instantaneous frequency for the signals recorded in planes 1 and 2. Changes in the slopes of the unwrapped phase and reversals of the frequency

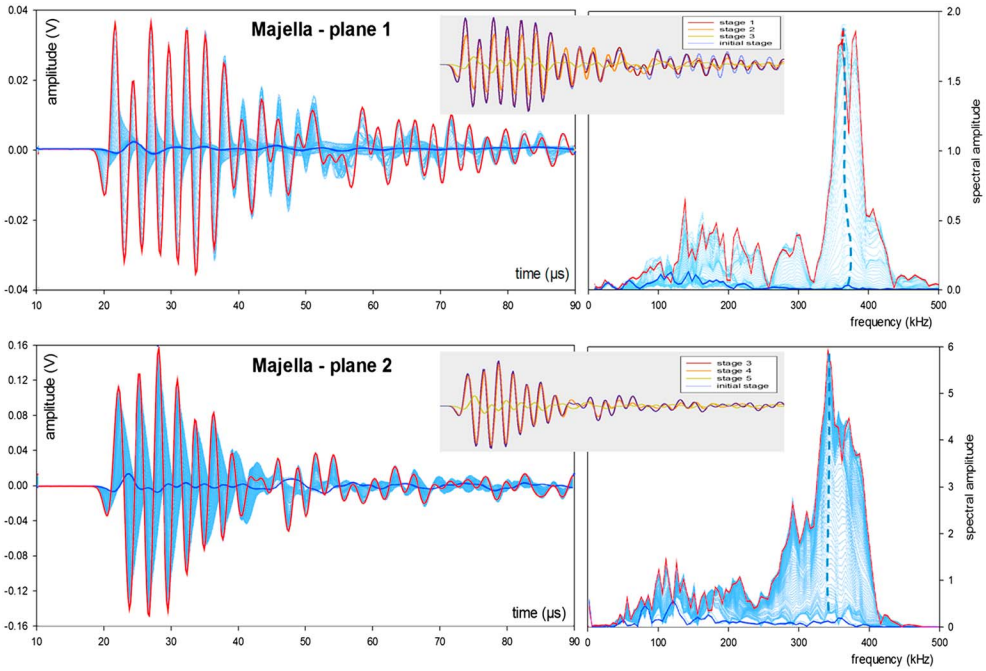

Figure 8. Plot of all the waveforms recorded during spontaneous water imbibition of the (left column) Majella grainstone and (right column) associated spectral amplitude for the transducers in (top row) plane 1 and (bottom row) plane 2. The red curves represent the initial stage (dry rock), and the dark blue curves represent snapshots 3 in plane 1 and snapshot 5 in plane 2. The inserted graphs show the waveforms corresponding to the five snapshots in Figure 6.

spikes are clearly visible; they are used to separate the signal into adjacent time domains corresponding to different wavelet arrivals recorded in a given waveform. The reconstructed signal after apodization is shown below, each wavelet being color labeled. Notice that there is a small overlap of the wavelets because of the use of apodization windows slightly larger than the one of the wavelet in the time domain. This overlap was done in purpose to avoid loss of information.

The duration and frequency of the five wavelet packets identified for the Sherwood sandstone are reported in Table 2. Whereas the instantaneous frequencies of the wavelets are similar for planes 1 and 2, the wavelet

Table 2. Main Attributes of the Wavelet Packets Identified in the Waveforms for the Dry Rocks Before the Imbibition Starts

	Sherwood Sandstone					Majella Grainstone				
	Wavelet Packet Number	Instantaneous Frequency (kHz)	Start Time (μs)	End Time (μs)	Number of Periods	Wavelet Packet Number	Instantaneous Frequency (kHz)	Start Time (μs)	End Time (μs)	Number of Periods
Plane 1	1	200	22	33	2.2	1	250	18	24	1.5
	2	310	33	67	10.5	2	370	24	36	4.4
	3	210	67	97	6.3	3	305	36	48	3.7
	4	160	97	140	6.9	4	220	48	57	2.0
	5	50	140	175	1.8	5	305	57	97	12.2
						6	260	97	118	5.5
						7	170	118	175	9.7
Plane 2	1	220	23	29	1.3	1	240	18	25	1.7
	2	370	29	50	7.8	2	360	25	42	6.1
	3	270	50	59	2.4	3	280	42	57	4.2
	4	140	59	129	9.8	4	250	57	68	2.8
	5	50	129	175	2.3	5	220	68	89	4.6
						6	180	89	129	7.2
						7	170	129	175	7.8

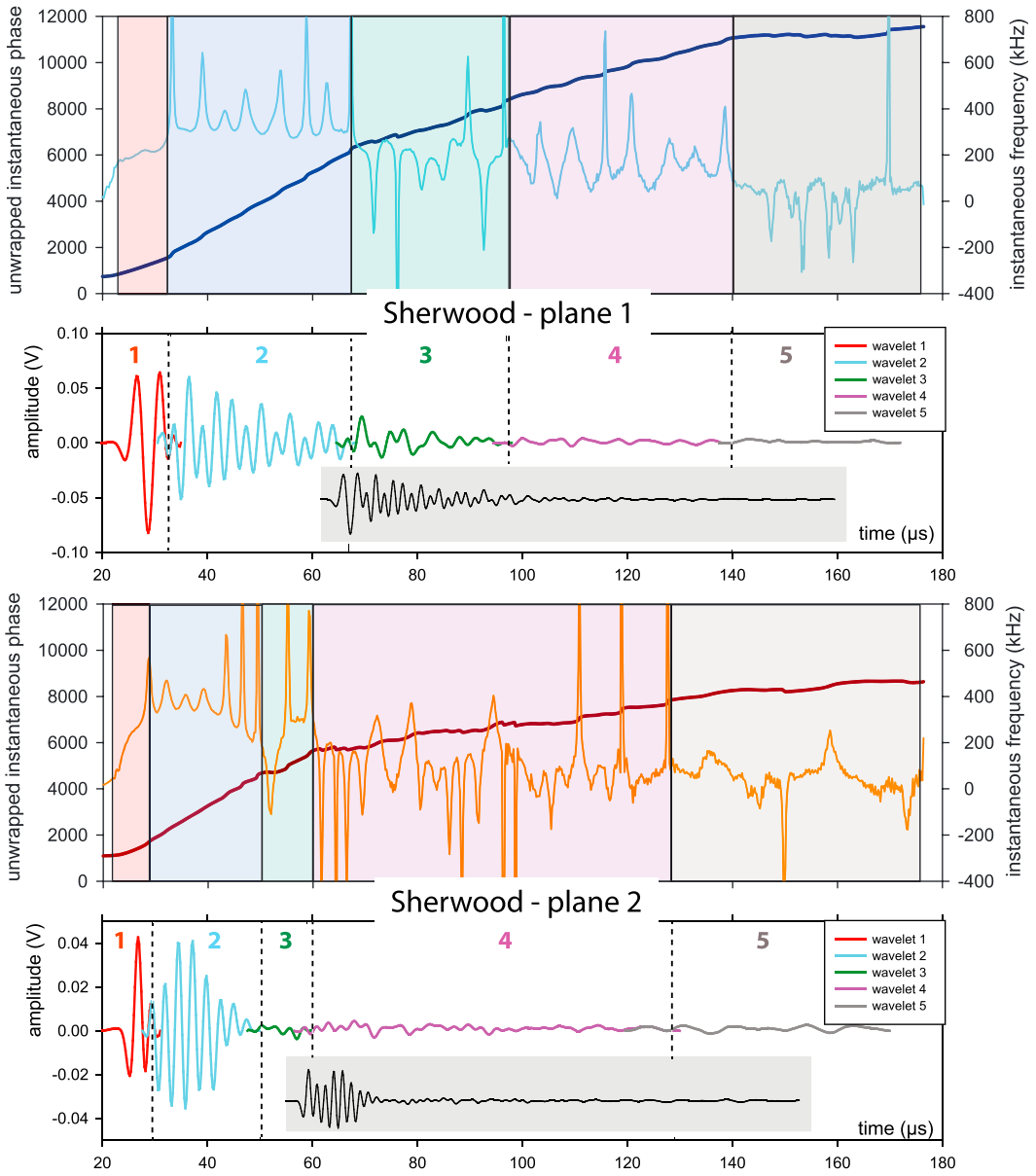

Figure 9. Wavelet packets identification for the Sherwood sandstone in each plane. Each wavelet packet and associated time interval is represented in a different color. The instantaneous frequencies (thin lines) are derived from the unwrapped instantaneous phase (thick lines). The initial waveform is inserted for comparison with the result of the wavelet reconstruction.

durations are noticeably different. This is consistent with the earlier observation that the recorded waveforms and associated spectra are also noticeably different in the two planes (Figure 7).

4.3.2. Majella Grainstone

Figure 10 presents the unwrapped instantaneous phase and the instantaneous frequency for the signals recorded in planes 1 and 2. Again, changes in the slopes and reversals of the frequency spikes are clearly visible. The reconstructed signal after apodization is shown below, each wavelet and corresponding time interval being represented with a different color.

The duration and frequency for the seven wavelet packets identified in the Majella grainstone are reported in Table 2. Both the instantaneous frequencies and the durations of the wavelets for planes 1 and 2 are comparable. This is consistent with the earlier observation that the recorded waveforms and associated spectra are also similar in the two planes (Figure 8).

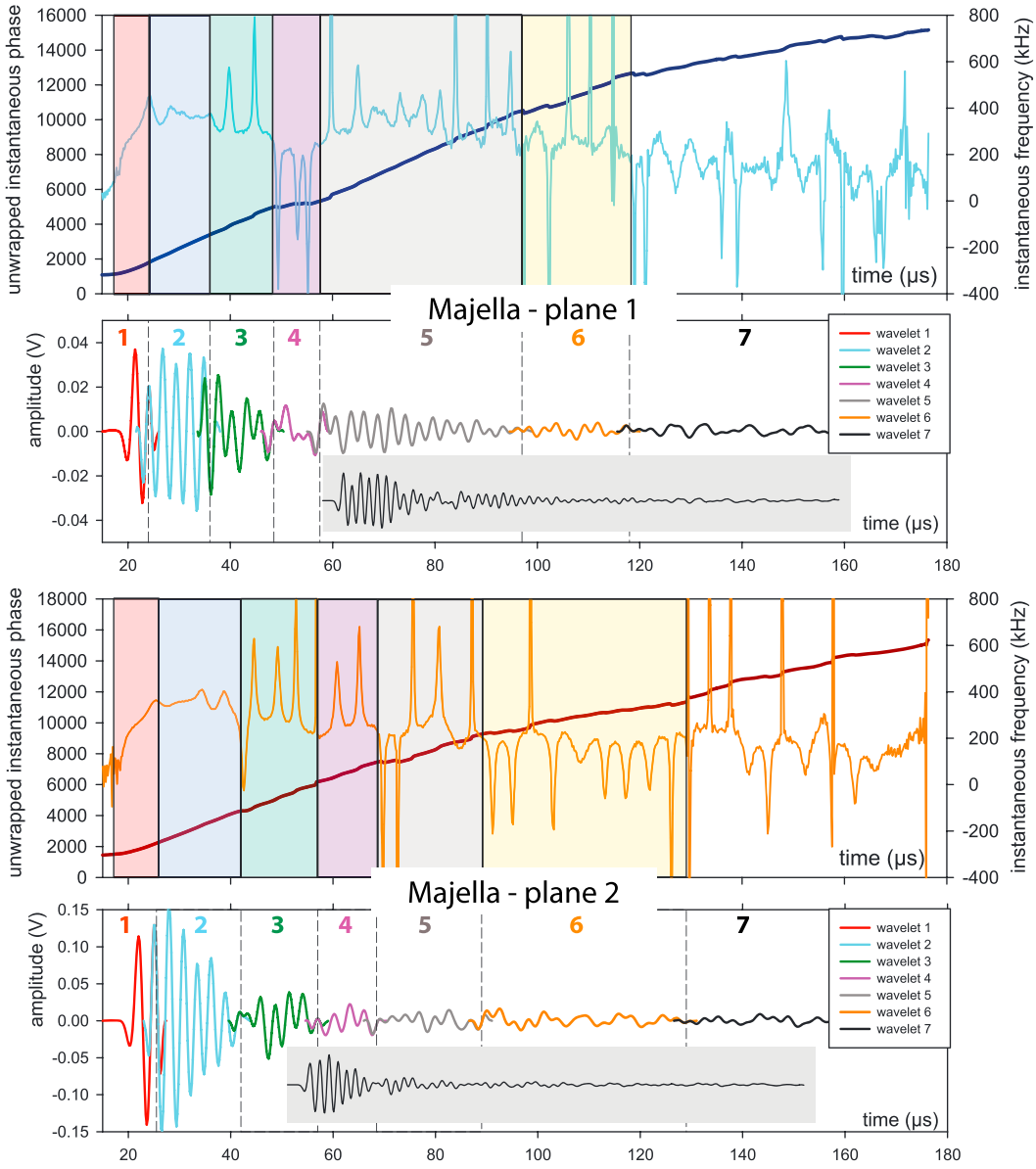

Figure 10. Wavelet packets identification for the Majella grainstone in each plane. Each wavelet and associated time interval is represented with a different color. The instantaneous frequencies (thin lines) are derived from the unwrapped instantaneous phase (thick lines). The initial waveform is inserted for comparison with the result of the wavelet reconstruction.

5. Discussion

Following our previous study on the Saint-Maximin grainstone and the Savonnières limestone [*David et al.*, 2015b], two new experiments have been conducted on the Sherwood sandstone and the Majella grainstone, to investigate the acoustic signature of a fluid moving within a porous rock during spontaneous imbibition with ultrasonic monitoring. These experiments confirm that monitoring the waveforms during imbibition in the laboratory is a powerful tool for detecting fluid motion in porous rocks. The combined X-ray imaging and ultrasonic monitoring permits to precisely identify the impact of capillary rise on the evolution of *P* wave attributes (velocity, amplitude, and spectral content): the position and geometry of the moving front can be assigned to each variation observed on one of these parameters. The study has been extended with a detailed analysis of the waveforms, showing the evolution of the spectral content and how the full waveforms can be decomposed into wavelets. To our knowledge, this is the first time that such a complete data

set combining rock physics, signal processing, and X-ray CT imaging is presented. Our observations raise also a number of questions that we will address in the following sections.

5.1. Sensitivity of Seismic Attributes to Fluid Motion

All the rocks tested so far share similarities in their behavior: the *P* wave amplitude (first peak) is impacted first by the approaching fluid, with a clear decrease when the maximum height of the fluid front is still well below (typically several millimeters) the direct wave path between the ultrasonic source and receiver. The variation of the *P* wave amplitude acts as a precursor of the approaching fluid. This amplitude decrease is always sharper for plane 1 compared to plane 2, which is consistent with the diffusive nature of the capillary rise of a fluid in the pore space. This is also consistent with the decreasing speed of spontaneous imbibition often observed in porous rocks, i.e., faster rise at the start, slowing down with time, and finally, vanishing when capillary and gravity forces cancel each other. Similar results were obtained by *Wulff and Mjaaland* [2002] in their imbibition/flooding experiments on Cleebourg sandstone. Their Figure 5 shows that (i) attenuation variations can be significantly larger than velocity variations, and (ii) attenuation is impacted before velocity is. Note that in their data set, the relative variation of the *S* wave velocity follows a trend similar to that of the *P* wave attenuation.

The *P* wave velocity drop occurs always after the amplitude decrease, with a magnitude always lower. It also systematically correlates with the arrival of the water front either in the Fresnel zone or in the transducers zone (Figures 5 and 6). We therefore recommend for similar applications to estimate the extent of the Fresnel clearance zone using equation (4) in order to define the minimum distance to the array of sensors available at which *P* waves become sensitive to the approaching fluid front. The decrease of *P* wave velocity during imbibition can be explained by the expected dependence of velocity on saturation as reported by *Dautriat et al*. [2016] for the Sherwood sandstone and by others on various rocks [*Mavko et al*., 2009; *Lopes et al*., 2012]. In water imbibition experiments, the variation of *P* wave velocity is either decreasing or increasing, depending on the competing effects of density increase (water replaces air) and bulk modulus increase [*Mavko et al*., 2009]. Capillary rise leads to the partial saturation of the rock, which results in our experiments in a lower *P* wave velocity. Note that depending on the nature of the injected fluid, a *P* wave velocity increase can also be observed (e.g., oil drainage experiments in the Sherwood sandstone [*David et al*., 2015a]).

The spectral content of the waveforms is also strongly sensitive to fluid motion (Figures 7 and 8). We did not observe a shift of the main frequency peak toward lower frequencies but a continuous extinction of the higher frequency peak amplitude until it becomes comparable or even smaller than the low-frequency peaks also present in the signal from the beginning. Overall, the imbibing rock acts as a low-pass filter on the propagating *P* wave. As a consequence, the relative weight of the low frequencies on the overall spectral content of the ultrasonic signal transmitted increases. With time of imbibition, this shifts the apparent dominant frequency of the transmitted signal toward the low-frequency end, without invoking a shift of the high-frequency peak itself. As expected and as shown by the wavelet analysis, the direct arrival of the propagating *P* wave is not affected by the reflections recorded in the waveform coda. This also shows that the results reported so far are not affected by the specific boundary conditions under which the experiment and measurements were conducted.

5.2. Elastic Weakening Through Water Imbibition

For both rocks in this study variations in amplitude occurred when the fluid front was well below the Fresnel clearance zone. The early changes in amplitude can likely be explained by water vapor adsorption which weakens the rock [*Clark et al*., 1980; *Pimienta et al*., 2014] leading to amplitude drop before the liquid water visible in the X-ray CT images reaches the Fresnel zone, which then triggers the velocity decrease. Vapor adsorption on mineral grains within the pore space is known to lower the surface energy and therefore the elastic moduli, wave velocities, and amplitudes [e.g., *Johnson et al*., 1971; *Murphy et al*., 1984]. The water adsorption micromechanisms leading to elastic weakening and nonlinearity at low saturations have been discussed by *van den Abeele et al*. [2002]. As shown by *Pimienta et al*. [2014], the weakening effect of moisture adsorption on elastic properties is particularly high in loosely cemented granular rocks, which is precisely the case for the Sherwood sandstone and the Majella grainstone. Comparatively to these earlier studies, our results suggest that water adsorption on mineral grains has more impact on wave amplitude

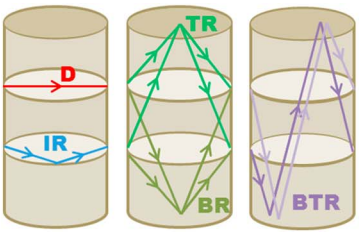

	arrival time (μs)	D	IR	BR	TR	BTR
Sherwood sandstone	plane 1	22.2 w1	31.0 w1 - w2	42.5 w2	82.5 w3	118.4 w4
	plane 2	23.4 w1	32.7 w2	77.1 w4	48.7 w2-w3	118.8 w4
Majella grainstone	plane 1	18.2 w1	25.4 w1 - w2	31.5 w2	59.4 w5	84.2 w5
	plane 2	18.4 w1	25.7 w1 - w2	54.9 w3	36.1 w2	84.6 w5

Figure 11. Wave propagation paths considered for the theoretical calculation of traveltimes between ultrasonic sources and receivers in planes 1 and 2. Each wave is associated to one or two wavelet packets defined in Figures 9 and 10. D: direct wave, IR: in-plane reflection, BR: bottom reflection, TR: top reflection, BTR: bottom and top reflections.

than it has on wave velocity. An extended data compilation providing clues that moisture diffusion accounts for the early amplitude drop that is presented in a companion paper in this special volume [*David et al.*, 2017].

5.3. Sensitivity of Wavelet Analysis

Based on the analysis of the analytical signal, the instantaneous phase, and the frequency (Figures 9 and 10), the waveforms recorded on the dry samples before imbibition were decomposed into wavelet packets: five for the Sherwood sandstone and seven for the Majella grainstone. Some of these wavelet packets can be interpreted in terms of specific wave propagation patterns in the rock samples, like reflections on boundaries. More complexity in the waveforms is expected in the presence of heterogeneities at the sample scale. Several raypaths of body waves were considered (Figure 11) with an increasing number of reflections, for which the theoretical traveltimes were calculated. Note that in addition to body waves, the coda waveform probably includes signals related to surface waves as well [*Adam et al.*, 2013] which will not be considered in the following calculation. The *P* wave anisotropy needs to be taken into account: here both rocks are assumed to be transversely isotropic (TI) media for sake of simplicity. Our unpublished measurements show that the TI approximation is verified for the Sherwood sandstone but is less relevant for the Majella grainstone [*Baud et al.*, 2009]. Furthermore, a simplified type of elliptical transverse isotropy is assumed ($\varepsilon = \delta$ using *Thomsen's* [1986] notation). For a raypath with angle θ with respect to the transverse isotropy axis, which is assumed to be orthogonal to the bedding plane, the *P* wave velocity $V_p(\theta)$ is given by

$$V_p(\theta) = V_o\left(1 + \varepsilon \sin^2\theta\right) \tag{5}$$

where V_o is the velocity normal to the isotropy plane and ε is the *P* wave anisotropy parameter which can be calculated from V_o which was measured along the sample axis and $V_p(90^\circ)$ measured along the bedding plane with both pairs of sensors used in our experiments. For the tested samples we obtain $\varepsilon = 0.24$ for the Sherwood sandstone and $\varepsilon = 0.16$ for the Majella grainstone. For the calculation of the traveltimes, the seismic raypaths are assumed to be straight lines. Five types of raypaths are considered (Figure 11): (D) direct waves, (IR) in-plane reflected waves, (BR) waves reflected once at the bottom end face of the rock sample, (TR) waves reflected once at the top end face of the rock sample, and (BTR) double reflection at the bottom then at the top end faces. We expect that BR and BTR will be impacted in the early stages of the fluid capillary rise compared to the other raypaths. Other raypaths with multiple reflections exist, but for sake of clarity, they are not considered in the following analysis. The traveltimes are given in Figure 11 for each rock and transducers plane. Taking into account the time intervals corresponding to the identified wavelet packets (Table 2), each raypath was assigned a wavelet packet. Wavelet 1 always represents the direct wave. The arrival time of the in-plane reflection corresponds to the transition between wavelet packets 1 and 2. The single reflections BR and TR are mostly represented by wavelet packets 3 and 4 and sometimes also 2. Finally, the double reflection BTR is represented by either wavelet packet 4 or 5. Higher-order wavelet packets found in the Majella grainstone correspond to multiple reflections.

Such a classification can then be used to predict which wavelets will first be impacted by the fluid capillary rise: wavelet packets of order higher than 3 should "see" the moving fluid front before wavelet packets of lower order.

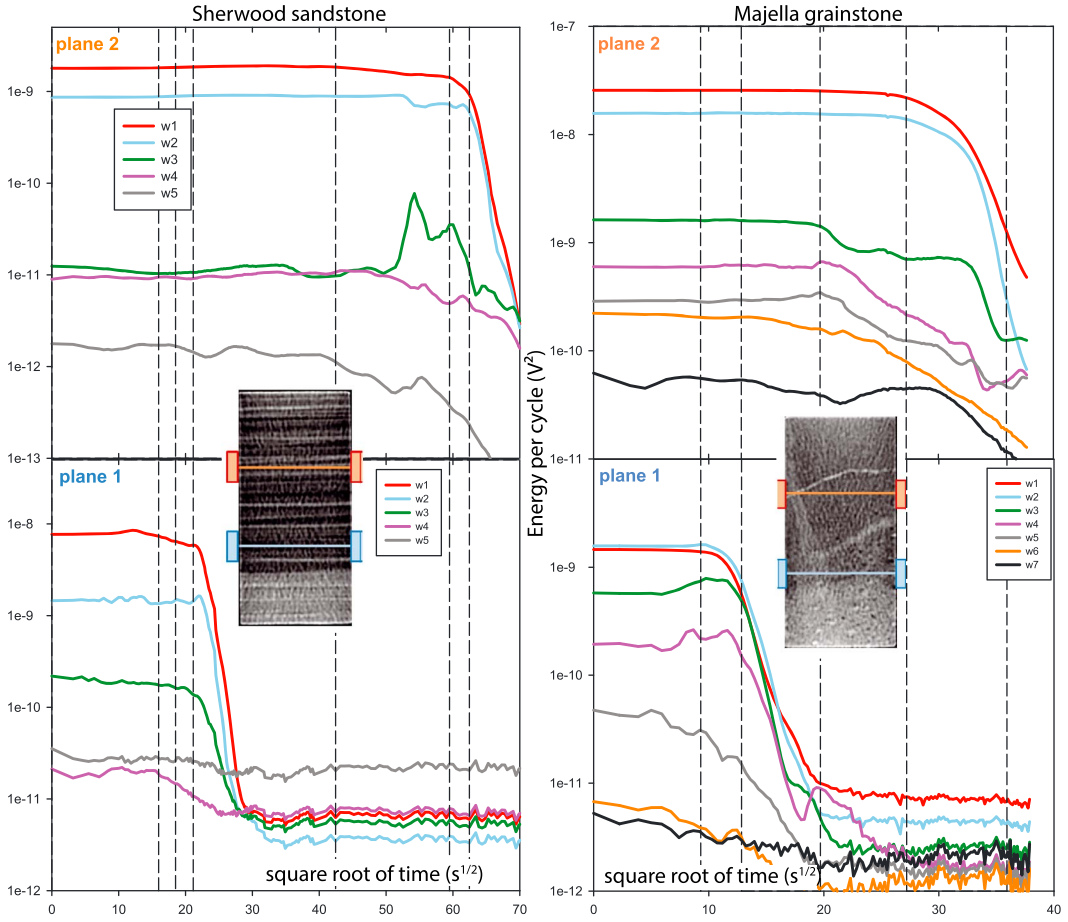

Figure 12. Energy per cycle calculated for each wavelet packet identified in Figures 9 and 10 (same color coding) versus square root of time during the spontaneous imbibition experiments on Sherwood sandstone and Majella grainstone. The vertical dashed lines are the same as in Figures 5 and 6.

To quantify this effect, the energy per cycle (or period) E_i is calculated for each wavelet packet w_i while imbibition proceeds

$$E_i = \frac{1}{N_c}\int (w_i(t))^2 dt \tag{6}$$

where N_c is the number of periods in the wavelet which can be estimated from the instantaneous frequency and the duration of the waveform (Table 2). The time integral in s (6) is taken over the duration of each wavelet. Figure 12 shows the evolution of the energy for each wavelet packet versus the square root of time (similar to Figures 5 and 6). We observe that

1. Wavelet packets 1 and 2 carry most of the energy, and the information they carry is essentially similar to the one obtained from the first peak amplitude analysis, which supports further the methodology developed here. Notice, however, that for the Sherwood sandstone—plane 1, some energy fluctuations occur for wavelet packets 1 and 2 before the first peak amplitude starts to decrease.
2. For higher-order wavelets, the overall behavior is more complex. The results for plane 1 in both rocks clearly show that these wavelets are impacted before any energy/amplitude decrease is recorded in the direct *P* wave, often as soon as contact is established between the water and the bottom end face of the rock sample. This is consistent with the assumption that these wavelets emanate from the source after multiple reflections. Therefore, these wavelets probe the lower part of the rock sample. The energy versus time evolution for these late wavelets (also known as waveform coda) is able to provide a precursor signal for the arrival of the fluid substitution front.
3. For the Sherwood sandstone—plane 2 a sudden increase of the energy for wavelet packet 3 and a drop of the energy for wavelet packet 2 are observed at about 50 $s^{1/2}$. This seems to occur when a jump in the

water level rise occurs (Figure 5a), suggesting that the imbibition process is not smooth in the Sherwood sandstone because of the horizontal layering, alternating denser and more porous layers. The data show that this discontinuous hydrodynamic process impacts the evolution of the elastic properties as well.

Our study shows that the decomposition of the recorded waveforms into wavelet packets is a powerful tool which provides useful information on the dynamics of fluid substitution investigated through ultrasonic waves sounding. In particular, the analysis of the higher-order wavelet packets and their energy variations as recorded in the waveform coda provides valuable information on the fluid substitution process away from the volume of rock probed by the direct wave. The strong sensitivity of coda waves to tiny changes in rock properties (fluid content in our case) is in good agreement with the results reported by *Adam et al*. [2013] on time-lapse seismic monitoring of dissolution processes in basalts.

6. Conclusions

Simultaneous X-ray CT imaging and ultrasonic monitoring of fluid substitution processes in porous rocks provide valuable information on the interplay between hydrodynamic processes and seismic properties. Our results on the Sherwood sandstone and the Majella grainstone confirm our previous findings on the Saint-Maximin grainstone and the Savonnières limestone: the amplitude of the first *P* wave arrival is impacted by the upward moving fluid front before the *P* wave velocity is, when the fluid front is still located well below the ultrasonic transducers plane. At this stage we suggest that amplitude is first impacted by water vapor adsorption, an issue which is further discussed in the companion paper in the same special volume [*David et al*., 2017]. The *P* wave velocity drop is triggered by the fluid front when it reaches the Fresnel clearance zone, an ellipsoidal volume including the source-receiver transducers and the direct raypath between them. The size of the Fresnel clearance zone as defined in the theory of wave propagation depends on the wavelength of the propagating wave. The spectral analysis of the waveforms shows that the amplitude of the high-frequency peak continuously decreases with imbibition time, without significant frequency shift. However, because the rock acts as a low-pass filter on the propagating waves, the low-frequency content of the transmitted wave becomes prominent with imbibition time, i.e., the overall spectral content of the transmitted wave appears to shift toward lower frequencies with imbibition time.

A wavelet analysis technique involving the analytical signal and the instantaneous phase has been devised to decompose the recorded waveforms into discrete wavelet packets. Each of them was quantitatively related to different wave paths involving direct *P* waves or single/multiple reflected waves on the sample boundaries. The first two wavelet packets recorded carry most of the energy and correspond to expected direct *P* wave or in-plane reflections. The evolution with time of the energy carried by these wavelet packets mimics that of the first peak amplitude. The energy carried by wavelet packets of higher order is sensitive to the fluid substitution process away from the direct raypath between the ultrasonic source-receiver pairs. This is attributed to the reflections of the primary source wavelet at the bottom boundary of the rock sample, where imbibition starts. A practical outcome of this study is that the energy distribution along the waveforms coda and its evolution during fluid migration can be used as a precursory warning of the approaching fluid front during fluid substitution processes. Future extension of this work will be to consider more realistic fluid substitutions at depth in reservoirs, e.g., water-oil substitution during enhanced oil recovery operations, at in situ pressure conditions. Another possible extension would be to apply the methodology to supercritical CO_2 injection into saline aquifers or depleted oil reservoirs.

Acknowledgments

We thank Delphine Bertauld for processing part of the data set and Claudio Delle Piane for obtaining the SEM images of the Majella grainstone. Many thanks to both reviewers and Associate Editor for helpful comments. All the data presented in this article are available in digital form upon request.

References

Adam, L., K. van Wijk, T. Otheim, and M. Batzle (2013), Changes in elastic wave velocity and rock microstructure due to basalt-CO_2-water reactions, *J. Geophys. Res. Solid Earth*, *118*, 4039–4047, doi:10.1002/jgrb.50302.

Akaike, H. (1974), Markovian representation of stochastic processes and its application to the analysis of autoregressive moving average processes, *Ann. Inst. Stat. Math.*, *26*(1), 363–387, doi:10.1007/BF02479833.

Avseth, P., T. Mukerji, and G. Mavko (2005), *Quantitative Seismic Interpretation: Applying Rock Physics Tools to Reduce Interpretation Risks*, 359 pp., Cambridge Univ. Press, Cambridge, U. K.

Barnes, A. E. (1992), The calculation of instantaneous frequency and instantaneous bandwidth, *Geophysics*, *57*(11), 1520–1524, doi:10.1190/1.1443220.

Baud, P., W. Zhu, and T. Wong (2000), Failure mode and weakening effect of water on sandstone, *J. Geophys. Res.*, *105*(B7), 16,371–16,389, doi:10.1029/2000JB900087.

Baud, P., S. Vinciguerra, C. David, A. Cavallo, E. Walker, and T. Reuschlé (2009), Compaction and failure in high porosity carbonates: Mechanical data and microstructural observations, *Pure Appl. Geophys.*, *166*(5–7), 869–898, doi:10.1007/s00024-009-0493-2.

Boashash, B., L. Boubchir, and G. Azemi (2012), A methodology for time-frequency image processing applied to the classification of non-stationary multichannel signals using instantaneous frequency descriptors with application to newborn EEG signals, *EURASIP J. Adv. Signal Process.*, *2012*(1), 117, doi:10.1186/1687-6180-2012-117.

Bourbié, T., O. Coussy, and B. Zinszner (1987), *Acoustics of Porous Media*, 334 pp., Technip, Paris.

Bracewell, R. (2000), *The Fourier Transform and Its Applications*, 3rd ed., 616 pp., McGraw-Hill, New York.

Červený, V., and J. E. P. Soares (1992), Fresnel volume ray tracing, *Geophysics*, *57*(7), 902–915, doi:10.1190/1.1443303.

Clark, V. A., B. R. Tittmann, and T. W. Spencer (1980), Effect of volatiles on attenuation (Q^{-1}) and velocity in sedimentary rocks, *J. Geophys. Res.*, *85*(B10), 5190-5198, doi:10.1029/JB085iB10p05190.

Cohen, L. (1995), *Time-Frequency Analysis*, 299 pp., Prentice-Hall, Engelwood Cliffs, N. J.

Dautriat, J., J. Sarout, C. David, D. Bertauld, and R. Macault (2016), Remote monitoring of the mechanical instability induced by fluid substitution and water weakening in the laboratory, *Phys. Earth Planet. Inter.*, *261*, 69–87, doi:10.1016/j.pepi.2016.06.011.

David, C., B. Menéndez, and J. M. Mengus (2011), X-ray imaging of water motion during capillary imbibition: Geometry and kinetics of water front in intact and damaged porous rocks, *J. Geophys. Res.*, *116*, B03204, doi:10.1029/2010JB007972.

David, C., J. Dautriat, J. Sarout, C. Delle Piane, B. Menéndez, R. Macault, and D. Bertauld (2015a), Mechanical instability induced by water weakening in laboratory fluid injection tests, *J. Geophys. Res. Solid Earth*, *120*, 4171–4188, doi:10.1002/2015JB011894.

David, C., D. Bertauld, J. Dautriat, J. Sarout, B. Menéndez, and B. Nabawy (2015b), Detection of moving capillary front in porous rocks using X-ray and ultrasonic methods, *Front. Phys.*, *3*, 53, doi:10.3389/fphy.2015.00053.

David, C., J. Sarout, J. Dautriat, L. Pimienta, M. Michée, M. Desrues, and C. Barnes (2017), Ultrasonic monitoring of spontaneous imbibition experiments: Precursory moisture diffusion effects ahead of water front, *J. Geophys. Res. Solid Earth*, *122*, 4948–4962, doi:10.1002/2017JB014193.

Digby, P. J. (1981), The effective elastic moduli of porous granular rocks, *J. Appl. Mech.*, *48*(4), 803, doi:10.1115/1.3157738.

Doornhof, D., G. K. Tron, N. B. Nagel, P. D. Pattillo, and C. Sayers (2006), Compaction and subsidence, *Oilfield Rev.*, *18*(3), 50–68.

Hadizadeh, J., and R. D. Law (1991), Water-weakening of sandstone and quartzite deformed at various stress and strain rates, *Int. J. Rock Mech. Min. Sci.*, *28*(5), 431–439.

Hsu, M.-K., J.-C. Sheu, and C. Hsue (2011), Overcoming the negative frequencies—Instantaneous frequency and amplitude estimation using osculating circle method, *J. Mar. Sci. Technol.*, *19*(5), 514–521.

JafarGandomi, A., and A. Curtis (2011), Detectability of petrophysical properties of subsurface CO_2-saturated aquifer reservoirs using surface geophysical methods, *Leading Edge*, *30*(10), 1112–1121, doi:10.1190/1.3657069.

Jaya, M., S. Shapiro, D. Bruhn, E. Huenges, and Ó. Flóvenz (2008), Temperature-dependent fluid substitution analysis of geothermal rocks at in-situ reservoir conditions, in *SEG Technical Program Expanded Abstracts 2008*, pp. 1774–1778, Society of Exploration Geophysicists, Las Vegas.

Johnson, K. L., K. Kendall, and A. D. Roberts (1971), Surface energy and the contact of elastic solids, *Proc. R. Soc. London, Ser. A*, *324*(1558), 301–313.

Lopes, S., M. Lebedev, S. Lopes, and M. Lebedev (2012), Laboratory study of the influence of changing the injection rate on P-wave velocities and water saturation in a limestone, *ASEG Ext. Abstr.*, *2012*(1), 1, doi:10.1071/ASEG2012ab083.

Lopes, S., M. Lebedev, T. M. Müller, M. B. Clennell, and B. Gurevich (2014), Forced imbibition into a limestone: Measuring P-wave velocity and water saturation dependence on injection rate, *Geophys. Prospect.*, *62*(5), 1126–1142, doi:10.1111/1365-2478.12111.

Mavko, G., T. Mukerji, and J. Dvorkin (2009), *The Rock Physics Handbook—Tools for Seismic Analysis of Porous Media*, 2nd ed., 511 pp., Cambridge Univ. Press, Cambridge, U. K.

Mees, F., R. Swennen, M. Van Geet, and P. Jacobs (2003), Applications of X-ray computed tomography in the geosciences, *Geol. Soc. London, Spec. Publ.*, *215*(1), 1–6, doi:10.1144/GSL.SP.2003.215.01.01.

Murphy, W. F., K. W. Winkler, and R. L. Kleinberg (1984), Frame modulus reduction in sedimentary rocks: The effect of adsorption on grain contacts, *Geophys. Res. Lett.*, *11*(9), 805–808, doi:10.1029/GL011i009p00805.

Nagatani, Y., and R. O. Tachibana (2014), Multichannel instantaneous frequency analysis of ultrasound propagating in cancellous bone, *J. Acoust. Soc. Am.*, *135*(3), 1197–1206, doi:10.1121/1.4864464.

Nguyen, V. H., N. Gland, J. Dautriat, C. David, J. Wassermann, and J. Guélard (2014), Compaction, permeability evolution and stress path effects in unconsolidated sand and weakly consolidated sandstone, *Int. J. Rock Mech. Min. Sci.*, *67*, 226–239, doi:10.1016/j.ijrmms.2013.07.001.

Novakowski, K. S., and R. W. Gillham (1988), Field investigations of the nature of water-table response to precipitation in shallow water-table environments, *J. Hydrol.*, *97*(1), 23–32, doi:10.1016/0022-1694(88)90063-7.

Pimienta, L., J. Fortin, and Y. Gueguen (2014), Investigation of elastic weakening in limestone and sandstone samples from moisture adsorption, *Geophys. J. Int.*, *199*(1), 335–347, doi:10.1093/gji/ggu257.

Rasolofosaon, P., and B. Zinszner (2004), Laboratory petroacoustics for seismic monitoring feasibility study, *Leading Edge*, *23*(3), 252–258, doi:10.1190/1.1690898.

Rasolofosaon, P. N. J., and B. Zinszner (2012), Experimental verification of the petroelastic model in the laboratory—Fluid substitution and pressure effects, *Oil Gas Sci. Technol. – Rev. IFP Energ. Nouv.*, *67*(2), 303–318, doi:10.2516/ogst/2011167.

Risnes, R., M. V. Madland, M. Hole, and N. K. Kwabiah (2005), Water weakening of chalk—Mechanical effects of water-glycol mixtures, *J. Pet. Sci. Eng.*, *48*(1), 21–36, doi:10.1016/j.petrol.2005.04.004.

Rutter, E. H. (1972), The influence of interstitial water on the rheological behaviour of calcite rocks, *Tectonophysics*, *14*(1), 13–33, doi:10.1016/0040-1951(72)90003-0.

Spetzler, J., and R. Snieder (2004), The Fresnel volume and transmitted waves, *Geophysics*, *69*(3), 653–663, doi:10.1190/1.1759451.

Stanchits, S., S. Mayr, S. Shapiro, and G. Dresen (2011), Fracturing of porous rock induced by fluid injection, *Tectonophysics*, *503*(1), 129–145, doi:10.1016/j.tecto.2010.09.022.

Taner, M. T., F. Koehler, and R. E. Sheriff (1979), Complex seismic trace analysis, *Geophysics*, *44*(6), 1041–1063, doi:10.1190/1.1440994.

Thomsen, L. (1986), Weak elastic anisotropy, *Geophysics*, *51*(10), 1954, doi:10.1190/1.1442051.

Toksöz, M. N., D. H. Johnston, and A. Timur (1979), Attenuation of seismic waves in dry and saturated rocks: I. Laboratory measurements, *Geophysics*, *44*(4), 681–690, doi:10.1190/1.1440969.

Tondi, E., A. Rustichelli, A. Cilona, F. Balsamo, F. Storti, G. Napoli, F. Agosta, P. Renda, and M. Giorgioni (2016), Hydraulic properties of fault zones in porous carbonates, examples from central and southern Italy, *Ital. J. Geosci.*, *135*(1), 68–79.

van den Abeele, K. E.-A., J. Carmeliet, P. A. Johnson, and B. Zinszner (2002), Influence of water saturation on the nonlinear elastic mesoscopic response in Earth materials and the implications to the mechanism of nonlinearity, *J. Geophys. Res.*, *107*(B6), 2121, doi:10.1029/2001JB000368.

Wulff, A., and S. Mjaaland (2002), Seismic monitoring of fluid fronts: An experimental study, *Geophysics*, *67*(1), 221–229, doi:10.1190/1.1451622.